energies

MDPI

Article

Lyapunov-Function-Based Controller for Single-Phase NPC Quasi-Z-Source Inverter with 2ω Frequency Ripple Suppression

Sertac Bayhan [1,*] and Hasan Komurcugil [2]

[1] Qatar Environment and Energy Research Institute, Hamad Bin Khalifa University, Doha 34110, Qatar
[2] Department of Computer Engineering, Eastern Mediterranean University, Via Mersin 10, 99628 Famagusta, Turkey; hasan.komurcugil@emu.edu.tr
* Correspondence: sbayhan@hbku.edu.qa; Tel.: +974-4454-7188

Abstract: This paper proposes a high-performance control technique based on Lyapunov's stability theory for a single-phase grid-connected neutral-point-clamped quasi-impedance source inverter with LCL filter. The Lyapunov function based control is employed to regulate the inverter output current, whereas the proportional resonant controller is used to produce the reference of the inverter output current that is needed in the Lyapunov function based control. Use of proportional resonant controller ensures the zero steady-state error in the grid current. An important feature of the proposed Lyapunov function based control is the achievement of resonance damping without using a dedicated damping method. Furthermore, the modified simple boost control technique is proposed to eliminate the double-line frequency ripples in the quasi-impedance source inductor currents and minimize the double-line frequency ripples in the quasi-impedance source capacitor voltages. The proposed control technique considerably reduces the inverter size, weight, and cost as well as increases overall system efficiency since the required inductances and capacitances sizes are lower. Experimental results obtained from a 2.5 kW neutral-point-clamped quasi-impedance source inverter prototype are presented to validate the performance of the Lyapunov function based control technique.

Keywords: grid-connected inverter; Lyapunov stability; nonlinear controller; proportional resonant control

Citation: Bayhan, S.; Komurcugil, H. Lyapunov-Function-Based Controller for Single-Phase NPC Quasi-Z-Source Inverter with 2ω Frequency Ripple Suppression. *Energies* **2021**, *14*, 140. https://doi.org/10.3390/en14010140

Received: 29 April 2020
Accepted: 22 May 2020
Published: 29 December 2020

1. Introduction

The power electronic converters play significant role in converting unregulated dc power into regulated ac power in photovoltaic (PV) systems. Compared to the conventional two-level configurations, the multilevel inverters (MI)s are recently promising solution for PV applications due to their significant advantages such as high performance, lower total harmonic distortion (THD), less voltage stress on the passive and active components, and so forth. The neutral-point-clamped (NPC) inverter is one of the popular MI topologies that is employed in many industrial applications [1–3].

The main role of PV inverters is to convert unregulated dc power into regulated ac power. To do that, different power converter topologies, which are mainly divided into two main streams namely single-stage (dc-ac inverter) and dual-stage (dc-dc boost converter + dc-ac inverter), are employed in PV inverters. In the dual-stage topology, an additional dc-dc converter is required to boost the dc voltage to the desired level. However, inclusion of dc-dc converter increases the cost of overall system and control complexity. As a remedy to these problems, the NPC quasi-Z Source (qZS) inverter topologies are evolved as alternative solutions in PV systems. The main advantage of this topology is the ability to regulate the voltage fluctuations in a single-stage. In addition, this topology requires less number of switches compared to dual-stage topologies, which means lower costs [4–7].

The controller design is a challenging issue since it needs to meet several control objectives that include fast dynamic response, preferably zero steady-state error, high

stability, and low THD under various loads. To meet these objectives, many control techniques are proposed for grid-connected inverters like deadbeat control [8], model predictive control [9], repetitive control [10], and sliding mode control [11–13]. Among these control techniques model predictive control and deadbeat control are the most attractive control techniques due to their fast transient response and near-zero steady-state error. On the other hand, these control techniques are sensitive to parameter changes in the system model and to noise in the high sampling frequency. Therefore, these drawbacks should be taken into account when such control techniques are designed. Another control technique is the repetitive control that provides satisfactory steady-state performance with excellent harmonic rejection under the non-linear loads. However, the transient response of the repetitive control is very slow and its tracking accuracy is poor. Alternatively, sliding mode control provides fast transient response and simplicity in implementation for single-phase inverters. Furthermore, this control technique offers high stability against non-linear load conditions and is not sensitive to the parameters changes in the system. However, it suffers from the inherent drawback of chattering phenomenon because of the variable switching frequency that results in inaccuracy in the control loop, reasonably high switching losses, and complexity in the filter design. Although each proposed control technique has its own advantages and disadvantages, none of these control techniques assures the global stability of the closed-loop system against sudden perturbations which change the operating point of the system.

In the case of grid-connected LCL -filtered inverter systems, the controller design is even more complex due to the inherent resonance damping requirement. The resonance problem is usually solved by passive damping [14], or by the active damping method [11–13,15–20]. Passive damping is realized by connecting a passive resistor in series or in parallel with the LCL filter components. However, the passive damping method is outdated due to the additional power losses decreasing efficiency of the system. On the other hand, the active damping method is realized by emulating the dissipative resistor in the control method rather than connecting it physically. Hence, it is generally referred to as virtual-resistor (VR) based active damping. Generally, the active damping method is based on the multi-loop control method [11–13,15–17] and the filter based control method [18,19]. Although the latter requires fewer sensors, it is sensitive to parameter variations and disturbances. As mentioned in Reference [20], single loop controller designed for LCL-filtered grid-connected inverter system cannot offer satisfactory performance. Therefore, most of the existing control methods utilize either two [11,12,15] or three [13,16] control loops.

Lyapunov-function-based control has been proposed for various applications that include hybrid active filter [21], dc/dc converters [22], single-phase inverters [23–25]. The main idea behind the Lyapunov-function-based control is to determine a control law such that the rate of change of the Lyapunov function remains always negative. Since the considered NPC-qZSI is interfaced to the grid via *LCL* filter, the energy on the *LCL* filter can be used to define the Lyapunov function and implement the Lyapunov-function-based control easily. The proposed controller requires three reference functions for the ac-side variables (reference of the inverter current, grid current reference, and capacitor voltage reference). The capacitor voltage reference is computed by using the defined grid current reference via a differential equation. The reference of the inverter current is produced using a proportional resonant (PR) controller which processes the grid current error applied to its input. The consequence of utilizing PR controller is that zero grid current error can be achieved. It is well known that the qZS inverter has the ability to boost its dc input voltage by making use of shoot-through switching state which permits the switches to be turned on at the same inverter leg. Hence, shoot-through duty ratio of qZS network should be controlled. To control the shoot-through state, various control methods have been proposed that include the simple boost control, the maximum boost control, and the maximum constant boost control [26]. Although the simple boost control technique offers a lower modulation index and voltage gain over other control techniques, the implementation of this technique is easier than others [26,27].

Similar to the case of conventional single-phase inverter, the double-line frequency (2ω) pulsating power exist in the dc side of the single-phase NPC-qZSI that results in 2ω ripple on the qZS capacitor voltages and on the qZS inductor currents [28]. These 2ω ripple components should be eliminated or minimized considerably. To eliminate and minimize the 2ω ripple, passive and active damping techniques have been proposed [29,30]. However, the requirement of large inductances and capacitors (for passive techniques) or extra semiconductor switches (for active techniques) cause considerably increase of the inverter volume, weight, and cost [31]. As an alternative to these techniques, the existing simple-boost technique has been modified. The modified control technique not only regulates the shoot-through duty ratio, but also mitigates the 2ω power flow on the qZS network. Unlike the active damping method in Reference [29], the proposed ripple suppression method is based on passive damping which does not require additional switching devices. In Reference [30], the 2ω ripple suppression method is based on modifying the shoot-through duty ratio with the small variations which are obtained by processing the inductor current (i_{L1}) through low pass filtering and proportional-integral (PI) controller. However, the proposed ripple suppression method requires an additional voltage sensor only without using additional PI controller and low pass filter as in Reference [30].

The proposed control strategy has two control parts: dc-side control and ac-side control. While dc-side control achieves the control of quasi impedance network variables (inductor currents and capacitor voltages), the ac-side control achieves the control of grid current. In literature, there are only several studies which investigate the control of single-phase grid-connected three-level NPC-qZSI with LCL filter [5,6]. The control method proposed in Reference [5] is for single-phase three-level NPC-qZSI. While dc-side variables are controlled by using proportional-integral-derivative (PID) control, ac-side control is achieved by PR controller. However, there is no 2ω ripple elimination methodology in the dc-side control. Also, the proposed control method is verified by simulation results rather than experimental results. Furthermore, the switching frequency is selected as 100 kHz which is very high for a MI application. On the other hand, a three-phase grid-connected three-level NPC-qZSI topology is tested experimentally in Reference [6] in which the control of ac-side is not discussed at all. However, the authors proposed a new modulation technique for the shoot through. Comparing the proposed control strategy with the control strategies in References [5,6], the proposed control strategy offers important features such as 2ω ripple suppression in the dc-side inductor current, fast transient response both in the dc- and ac-side variables, strengthened stability, good tracking performance and zero grid current error in the steady-state. Nevertheless, a more detailed comparison of the ac-side is also provided in Section 4.

The major contributions of this paper include—(1) The ac-side of the NPC-qZSI is controlled by Lyapunov-function-based control which possesses many features such as fast dynamic response, strengthened stability, reduced number of sensors, excellent resonance damping without using dedicated active damping technique, guaranteed zero steady-state error and low THD in grid current. (2) The existing simple-boost control method in References [26,27] is modified to eliminate the 2ω power flow on the qZS inductances and minimize the 2ω power flow on the qZS capacitances. The proposed control technique considerably reduces the inverter size, weight, and cost as well as increases overall system efficiency.

In order to demonstrate the effectiveness of proposed control technique in the steady-state and during transient, experimental studies have been conducted through a small-scale NPC-qZSI prototype. The remainder of the paper is organized as follows. In Section 2.1, the modeling of the NPC-qZSI is presented. In Section 2.2 the proposed control strategies are introduced and extensively analyzed. In Section 3, the experimental results obtained from a 2.5 kW prototype are presented for different operating conditions. Finally, an appraisal of the proposed methodology is given in the conclusion.

2. Materials and Methods

2.1. Mathematical Modeling of NPC-qZSI

The single-phase grid-connected NPC-qZSI with *LCL* filter is shown in Figure 1 [3]. The input circuit of this inverter is built by an impedance source network that provides the ability to boost the input voltage at the required level. It is well-known that impedance source inverter has two switching states namely shoot-through and non-shoot-through states and the mathematical model of the NPC-qZSI depends on these switching states as depicted in Figure 2 [32]. The capacitors and inductors of the qZS network are assumed to be identical as follows [32]

$$L_1 = L_3, \;\; L_2 = L_4, \;\; C_1 = C_4, \;\; C_2 = C_3. \tag{1}$$

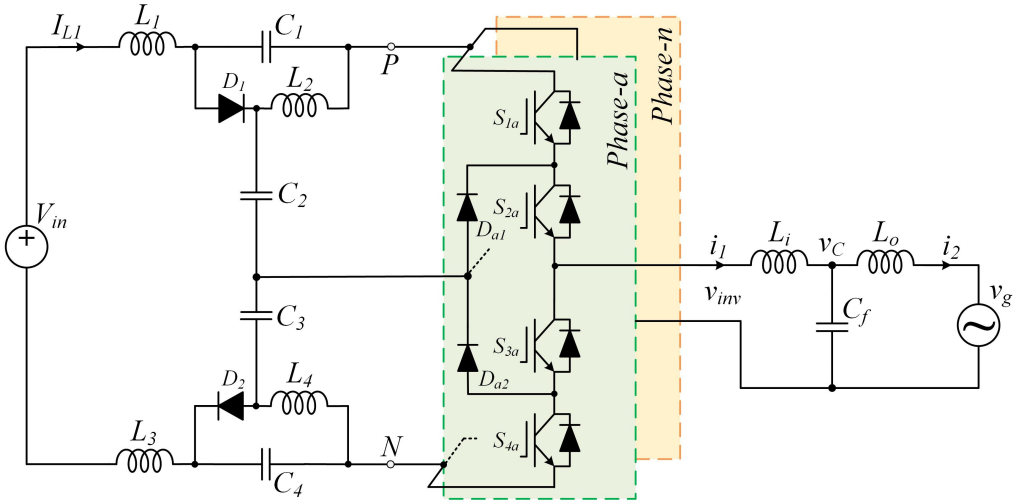

Figure 1. The Single-phase grid-connected NPC-qZSI with LCL filter [3,32].

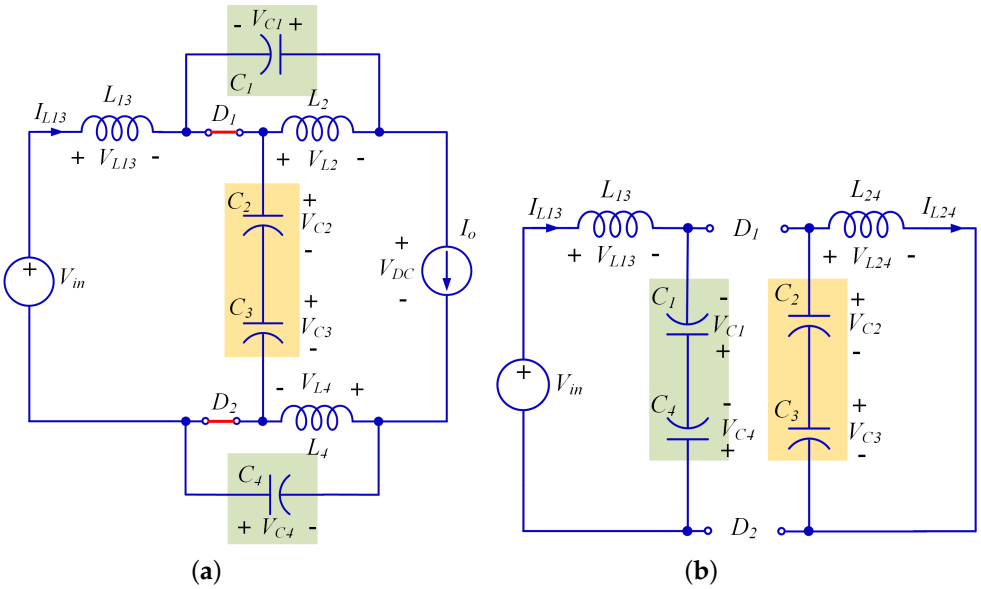

Figure 2. The model of qZS network. (**a**) in the non-shoot-through state; (**b**) in shoot-through state [32].

Although the values of capacitors and inductances can vary in practice, this variation is relatively small and has no influence on the performance of the proposed control method. This fact can be observed in the experimental results provided in Section 3 where theoreti-

cally identical capacitors and inductors are used which have almost no adverse effect on the performance of the proposed control method in practice. During non-shoot-through state, the NPC-qZSI is represented as a current source as shown in Figure 2a. The voltage across the inductors can be written as follows [32]

$$V_{L2} = -V_{C1}, \quad V_{L4} = -V_{C4}, \tag{2}$$

$$V_{L13} = V_{in} - V_{C2} - V_{C3}. \tag{3}$$

On the other hand, in shoot-through state, the NPC-qZSI is represented as short circuit as shown in Figure 2b. The voltage across the inductors can be written as [32]

$$V_{L13} = V_{in} + V_{C1} + V_{C4}, \tag{4}$$

$$V_{L24} = V_{C2} + V_{C3}. \tag{5}$$

From (2) to (5), inductor voltages are written as [32]

$$\begin{aligned} V_{L1} &= T_0\left(\tfrac{V_{in}+V_{C1}+V_{C4}}{2}\right) + T_1\left(\tfrac{V_{in}-V_{C2}-V_{C3}}{2}\right) = 0 \\ V_{L2} &= T_0\left(\tfrac{V_{C2}+V_{C3}}{2}\right) + T_1(-V_{C1}) = 0 \\ V_{L3} &= T_0\left(\tfrac{V_{in}+V_{C1}+V_{C4}}{2}\right) + T_1\left(\tfrac{V_{in}-V_{C2}-V_{C3}}{2}\right) = 0 \\ V_{L4} &= T_0\left(\tfrac{V_{C2}+V_{C3}}{2}\right) + T_1(-V_{C4}) = 0, \end{aligned} \tag{6}$$

where T_0 is the period of shoot-through whereas T_1 is the period of non-shoot-through states. By making use of (6), the capacitor voltages can be written as [32]

$$V_{C1} = V_{C4} = \frac{\mathbf{d}_{ST} V_{in}}{2 - 4\mathbf{d}_{ST}}, \quad V_{C2} = V_{C3} = \frac{(1 - \mathbf{d}_{ST}) V_{in}}{2 - 4\mathbf{d}_{ST}}, \tag{7}$$

where $\mathbf{d}_{ST}$ is duty-cycle of the shoot-through state. Applying Kirchhoff's voltage law to the second loop involving capacitor voltages in Figure 2a, the expression of dc-link voltage V_{PN} can be obtained as follows [32]

$$V_{PN} = V_{C1} + V_{C2} + V_{C3} + V_{C4}. \tag{8}$$

The boost factor (B) is written as

$$B = \frac{V_{PN}}{V_{in}} = \frac{V_{C1} + V_{C2} + V_{C3} + V_{C4}}{V_{in}} = \frac{1}{1 - 2\mathbf{d_{ST}}}. \tag{9}$$

It is worth noting that the correctness of the Equations (1)–(9) is already verified in the literature [3,6,7]. This clearly shows the validity of the models in Figure 2. The inverter output voltage (v_{inv}) and current (i_1) are

$$v_{inv} = \sqrt{2} V_{inv} \sin \omega t, \quad i_1 = \sqrt{2} I_1 \sin(\omega t - \theta), \tag{10}$$

where ω is the fundamental angular frequency, θ is the phase angle, V_{inv} and I_1 are the rms output voltage and current, respectively. The inverter output power is written as

$$P_o = V_{inv} I_1 \cos\theta - V_{inv} I_1 \cos(2\omega t - \theta). \tag{11}$$

Equation (11) shows that output power has two components which flow through

dc and ac sides of the inverter. The first component of the equation represents active power and the second component is the 2ω power that causes fluctuations (ripples) on voltages and currents in the dc-side of the qZSI. The frequency of this ripple is 2ω. These ripples, unfortunately, cannot be eliminated completely because of the inherent nature of the single-phase inverter. However, the impact of the 2ω ripples can be minimized through some design and/or control approaches.

2.2. The Proposed Control Technique

The block diagram of the control structure is given in Figure 3. The proposed control technique handles the grid current (i_2) control and the dc-link voltage (V_{PN}) regulation with 2ω power flow mitigation. These control objectives are described in detail as follows.

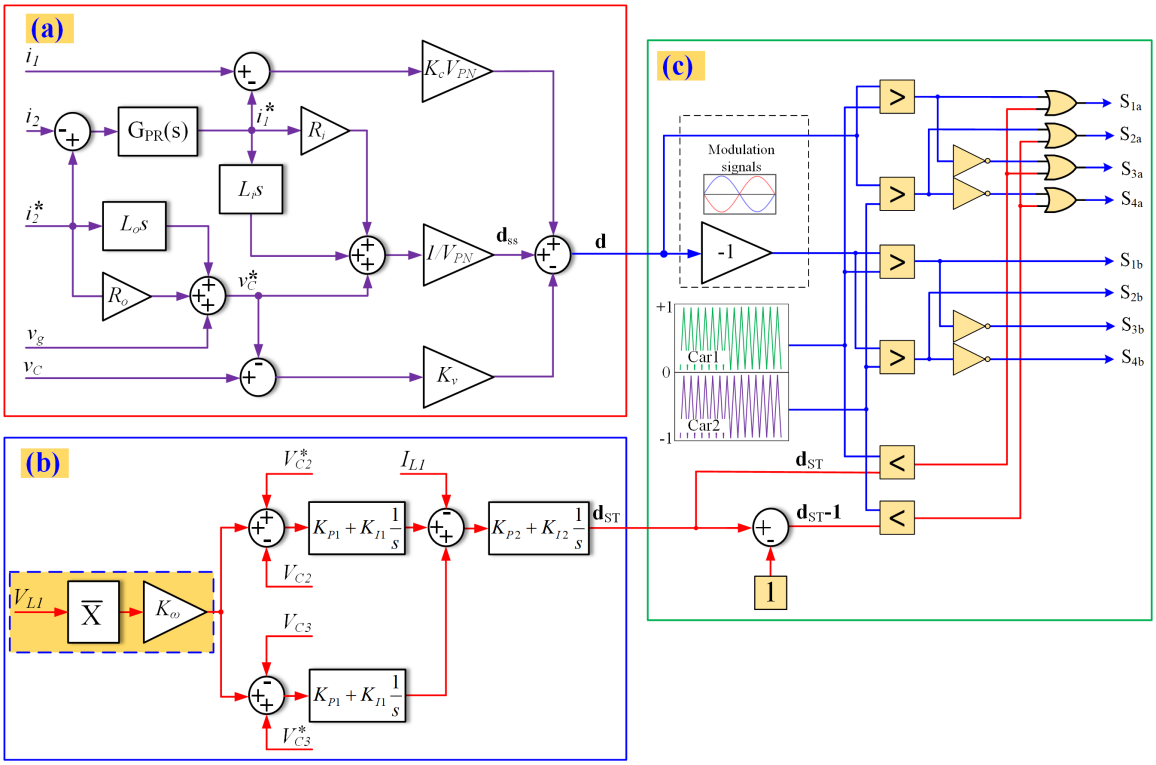

Figure 3. The block diagram of the developed control technique; (**a**) Lyapunov-function based control for ac-side variables; (**b**) dc-side control with 2ω ripple suppression; (**c**) Gate signal generation.

2.2.1. Control of AC-Side Variables

To control the grid current (i_2), the Lyapunov-function-based control technique is utilized. It is worth noting that the derivative of Lyapunov function should be guaranteed in this control technique. The determination of the Lyapunov function is usually based on the energy dissipation of the system under consideration. More detailed information about Lyapunov function is available in [23–25,33].

Now, let the Lyapunov function be defined as follows

$$V(x) = 0.5L_i x_1^2 + 0.5L_o x_2^2 + 0.5C_f x_3^2, \tag{12}$$

where x_1, x_2, and x_3 are the state variables defined as

$$x_1 = i_1 - i_1^* \quad x_2 = i_2 - i_2^* \quad x_3 = v_C - v_C^*, \tag{13}$$

where i_1, i_2, and v_C represent the inverter output current, the grid current, and the filter capacitor voltage, respectively. The reference values of these variables are marked with '*'

superscript symbol. It can be seen from (12) that the Lyapunov function $V(x)$ contains terms which are the energy stored in the LCL filter components (L_i, L_o, and C_f). The derivative of $V(x)$ is given by

$$\dot{V}(x) = x_1 L_i \dot{x}_1 + x_2 L_o \dot{x}_2 + x_3 C_f \dot{x}_3. \tag{14}$$

Using the voltage and current laws of Kirchhoff, the following expressions can be obtained with the circuit model

$$L_i \frac{di_1}{dt} + R_i i_1 = v_{inv} - v_C, \tag{15}$$

$$L_o \frac{di_2}{dt} + R_o i_2 = v_C - v_g, \tag{16}$$

$$C_f \frac{dv_C}{dt} = i_1 - i_2, \tag{17}$$

where v_g denotes the grid voltage , v_C denotes the filter capacitor voltage, and v_{inv} is the inverter output voltage. Furthermore, R_i and R_o are the the resistance of the filter inductances L_i and L_o. The output voltage of the inverter can be defined in terms of dc input voltage as follows

$$v_{inv} = \mathbf{d} V_{PN}, \tag{18}$$

where $\mathbf{d}$ represents the switching function defined as a combination of its steady-state and perturbed terms as

$$\mathbf{d} = d_{ss} + d_p. \tag{19}$$

The expression of switching function in the steady-state can be obtained from (15) with the assumption that $i_1 = i_1^*$ and $v_c = v_C^*$

$$d_{ss} = \frac{1}{V_{PN}} \left(L_i \frac{di_1^*}{dt} + R_i i_1^* + v_C^* \right). \tag{20}$$

Now, substituting (13) into (15)–(17) results in

$$L_i \dot{x}_1 = d_p V_{PN} - R_i x_1 - x_3, \tag{21}$$

$$L_o \dot{x}_2 = x_3 - R_o x_2, \tag{22}$$

$$C_f \dot{x}_3 = x_1 - x_2. \tag{23}$$

where $\dot{x}$ represents the time derivative of x. Now, substituting (21)–(23) into (14) yields

$$\dot{V}(x) = d_p V_{PN} x_1 - R_i x_1^2 - R_o x_2^2. \tag{24}$$

It is evident from (24) that $\dot{V}(x)$ is always negative if d_p is selected as

$$d_p = K_c V_{PN} x_1, \tag{25}$$

where $K_c < 0$. The overall switching function can be written by combining (20) and (25) as

$$\mathbf{d} = \frac{1}{V_{PN}} \left(L_i \frac{di_1^*}{dt} + R_i i_1^* + v_C^* \right) + K_c V_{PN} x_1. \tag{26}$$

The capacitor voltage reference in (26) is defined as

$$v_C^* = L_o \frac{di_2^*}{dt} + R_o i_2^* + v_g. \tag{27}$$

The reference for the inverter current (i_1^*) can be computed using $i_1^* = i_c^* + i_2^*$ where $i_c^* = C_f dv_C^*/dt$. However, i_c^* would be computed inaccurately when L_o, R_o, and C_f deviate from their actual values. In this case, i_1^* will be inaccurate as well which leads to steady-state error in the grid current i_2. Hence, in order to avoid these problems, i_1^* is produced through a PR controller which uses the following transfer function

$$G_{PR}(s) = K_p + \frac{2K_r\omega_c s}{s^2 + 2\omega_c s + \omega^2}, \tag{28}$$

where K_p and K_r denote the proportional and resonant gains, ω_c denotes the cut-off frequency and ω denotes the resonant frequency. The transfer function $G_{PR}(s)$ produces i_1^* by processing the grid current error ($i_2^* - i_2$) applied to its input. As a consequence of using PR controller, not only i_1^* is generated accurately, but also i_2 tracks its reference in the steady-state with zero error. However, when (26) is used to control the ac-side variables (i_1, i_2, and v_C), the closed-loop system may not exhibit satisfactory response (or even may become unstable) since $\mathbf{d}$ does not contain capacitor voltage feedback. Therefore, the perturbed duty cycle in (25) is modified by adding the capacitor voltage loop as follows

$$d_p = K_c V_{PN} x_1 - K_v x_3, \tag{29}$$

where K_v is a constant. Now, the total switching function can be obtained as

$$\mathbf{d} = \frac{1}{V_{PN}}\left(L_i \frac{di_1^*}{dt} + R_i i_1^* + v_C^*\right) + K_c V_{PN} x_1 - K_v x_3. \tag{30}$$

The closed-loop transfer function which relates the reference grid current to actual grid current is an important tool in determining the behavior of the closed-loop system in the frequency domain. In order to investigate the performance of the closed-loop system at the worst case, the closed-loop transfer function is derived by neglecting R_i and R_o (since R_i and R_o provide passive damping). Now, substituting (30) into (15) yields

$$L_i \frac{di_1}{dt} = L_i \frac{di_1^*}{dt} + v_C^* + K_c V_{PN}^2 (i_1 - i_1^*) - K_v V_{PN}(v_C - v_C^*) - v_C. \tag{31}$$

The expressions for i_1 and v_C in terms of i_2 when $v_g = 0$ can be written as

$$i_1 = L_o C_f \frac{d^2 i_2}{dt^2} + i_2, \tag{32}$$

$$v_C = L_o \frac{di_2}{dt}. \tag{33}$$

Substituting (27), (32), and (33) into (31) results in

$$L_i C_f L_o \frac{d^3 i_2}{dt^2} - K_c V_{PN}^2 C_f L_o \frac{d^2 i_2}{dt^2} + L_i \frac{di_2}{dt} - K_c V_{PN}^2 i_2 = L_i \frac{di_1^*}{dt} - K_c V_{PN}^2 i_1^*. \tag{34}$$

The Laplace transform of (34) can be written as

$$I_2(s)\left(L_i C_f L_o s^3 - K_c V_{PN}^2 C_f L_o s^2 + L_i s - K_c V_{PN}^2\right) = I_1^*(s)\left(L_i s - K_c V_{PN}^2\right). \tag{35}$$

The Laplace transform of i_1^* can be written as

$$I_1^*(s) = (I_2^*(s) - I_2(s))\frac{K_p s^2 + 2\omega_c(K_p + K_r)s + K_p\omega^2}{s^2 + 2\omega_c s + \omega^2}. \tag{36}$$

Now, substituting (36) into (35) and collecting similar terms, one can obtain the transfer function from reference grid current to actual grid current as follows

$$H(s) = \frac{I_2(s)}{I_2^*(s)} = \frac{a_3 s^3 + a_2 s^2 + a_1 s + a_0}{b_5 s^5 + b_4 s^4 + b_3 s^3 + b_2 s^2 + b_1 s + b_0}, \tag{37}$$

where

$$\begin{aligned}
a_3 &= L_i K_p + L_o(1 + K_v V_{PN}) \\
a_2 &= 2\omega_c L_i(K_p + K_r) - K_p K_c V_{PN}^2 + 2\omega_c L_o(1 + K_v V_{PN}) \\
a_1 &= \omega^2 L_i K_p - 2\omega_c K_c V_{PN}^2(K_p + K_r) + \omega^2 L_o(1 + K_v V_{PN}) \\
a_0 &= -\omega^2 K_p K_c V_{PN}^2 \\
b_5 &= L_i C_f L_o \\
b_4 &= 2\omega_c L_i C_f L_o - C_f L_o K_c V_{PN}^2 \\
b_3 &= L_i + L_o + \omega^2 L_i C_f L_o - 2\omega_c C_f L_o K_c V_{PN}^2 + \\
&\quad L_i K_p + L_o K_v V_{PN} \\
b_2 &= 2\omega_c(L_i K_p + L_i K_r + L_i + L_o + L_o K_v V_{PN}) - \\
&\quad K_c V_{PN}^2(1 + K_p + \omega^2 C_f L_o) \\
b_1 &= \omega^2(L_i + L_o + L_i K_p + L_o K_v V_{PN}) - \\
&\quad 2\omega_c K_c V_{PN}^2(K_p + K_r + 1) \\
b_0 &= -\omega^2 K_c V_{PN}^2(1 + K_p).
\end{aligned}$$

The denominator of $H(s)$ constitutes the characteristic equation of the closed-loop system. All coefficients in the characteristic equation are positive constants, since $K_c < 0$, $K_v > 0$, $K_p > 0$, and $K_r > 0$. It is obvious from the characteristic equation that there are five poles. Locations of these poles determine the dynamic response of the closed-loop system. The root locus of the poles, obtained with the system parameters shown in Table 1 by varying K_c in the interval $[-0.0001, -0.003]$ while K_v is maintained at 0.875, 0.5, and 0.3, are shown in Figure 4. It can be seen that while three poles (p_1, p_2, p_3) are strongly affected from K_c and K_v, the other poles (p_4, p_5) are slightly affected from K_c and K_v. From Figure 4, it can be easily observed that when K_v is increased, while break-in point becomes larger, the break-away point decreases. Hence, as a consequence of varying K_c, all poles (including p_4 and p_5) move away from the imaginary axis until break-in point occurs. This means that K_c has the ability to move all poles away from the imaginary axis to some extent (until break-in point). Moving poles away from the imaginary axis, not only strengthens the stability, but also makes the dynamic response faster. However, when $|K_c|$ is increased further, while p_1 continues to move away from the imaginary axis, p_2 and p_3 change direction and move toward the imaginary axis as shown in Figure 4a,c,e. The other poles (p_4, p_5) also move away from the imaginary axis when $|K_c|$ is increased as shown in Figure 4b,d,f. But their effect on the dynamic response is limited. Although the system in (15)–(17) is linear, its control using a linear controller is a challenging issue due to the inherent resonance introduced by the *LCL* filter. That's why nonlinear controllers are widely used to achieve the desired performance for such inverter systems [4,8–10,12–15].

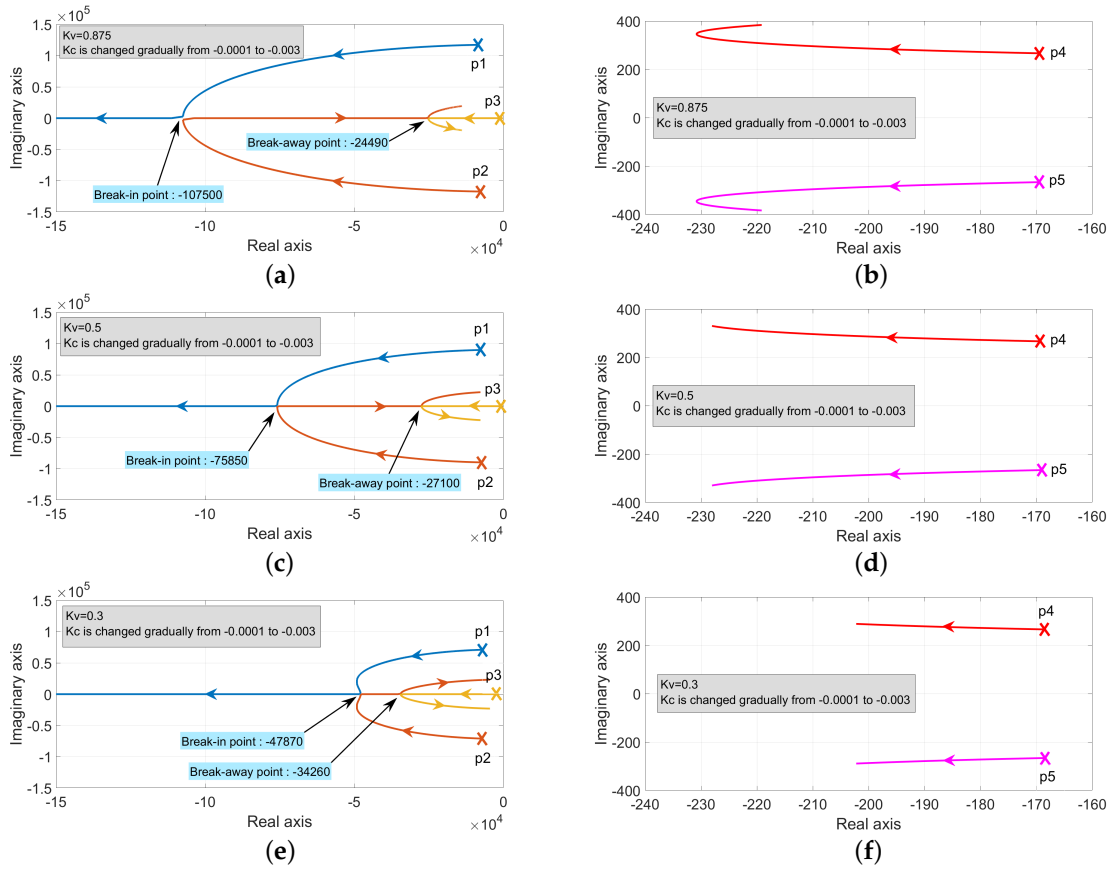

Figure 4. Root locus of closed-loop poles obtained when (**a**,**b**) K_c is varied with K_v = 0.875 , (**c**,**d**) K_c is varied with K_v = 0.5, and (**e**,**f**) K_c is varied with K_v = 0.3.

2.2.2. DC-Side Control with 2ω Ripple Suppression

In order to achieve the control of voltages (V_{C1}, V_{C2}, V_{C3}, and V_{C4}) and currents (I_{L1}, I_{L2}, I_{L3}, and I_{L4}) in the dc-side, the shoot-through duty cycle ($\mathbf{d}_{ST}$) should be controlled. Once, the control of V_{C2}, V_{C3}, and I_{L1} are accomplished successfully, the control of other dc variables are done automatically. In this study, the control of dc-side variables is achieved by using proportional-integral (PI) controllers. The inductor current reference I^*_{L1} is generated as follows

$$\begin{aligned} I^*_{L_1} &= K_{P1}(V^*_{C2} - V_{C2} + K_\omega \bar{V}_{L1}) + \\ & K_{I1} \int (V^*_{C2} - V_{C2} + K_\omega \bar{V}_{L1})dt + \\ & K_{P1}(V^*_{C3} - V_{C3} + K_\omega \bar{V}_{L1}) + \\ & K_{I1} \int (V^*_{C3} - V_{C3} + K_\omega \bar{V}_{L1})dt, \end{aligned} \tag{38}$$

where K_ω is a constant for 2ω ripple suppression and $\bar{V}_{L1}$ denotes the average of V_{L1}. The voltage across L_1 is measured by a voltage sensor and its average can be computed by using the built-in block available in the real time controller platform such as Dspace and OPAL-RT. In the conventional dc-side control, I^*_{L1} involves 2ω ripple which occurs on I_{L1} as a result of the applied control [24,28]. In order to suppress 2ω ripple on I_{L1}, it is required to produce I^*_{L1} without 2ω ripple. If I^*_{L1} does not involve 2ω ripple, then I_{L1} will not contain 2ω ripple provided that I_{L1} tracks I^*_{L1} successfully. Here, if $K_\omega \bar{V}_{L1}$ is fed back into $(V^*_{C2} - V_{C2})$ and $(V^*_{C3} - V_{C3})$, then I^*_{L1} can be produced without 2ω ripple. Figure 5 shows the simulation results of I_{L1} and I^*_{L1} without and with 2ω ripple suppression method.

Having generated I^*_{L1}, it can be used in the input of third PI controller to generate the shooth-through duty cycle as

$$\mathbf{d}_{ST} = K_{P2}(I^*_{L1} - I_{L1}) + K_{I2}\int (I^*_{L1} - I_{L1})dt. \tag{39}$$

Now, $\mathbf{d}_{ST}$ can be combined with $\mathbf{d}$ so that the desired pulse width modulation (PWM) signals for the switches of NPC-qSZI can be generated.

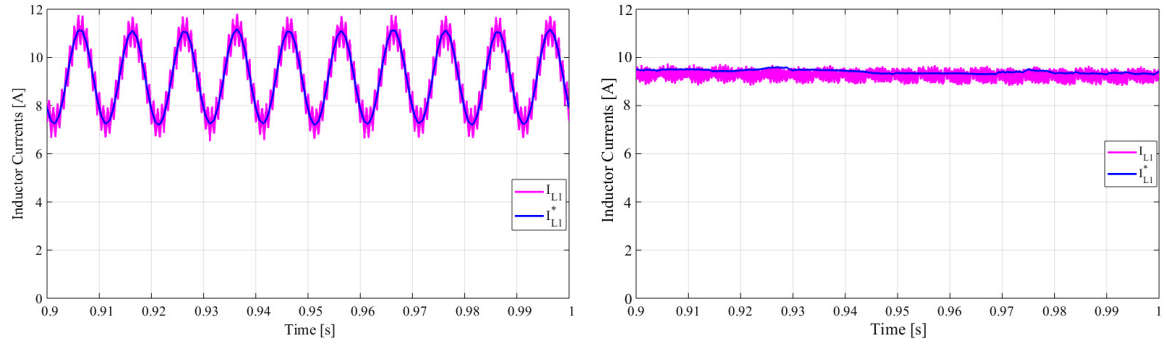

(**a**) (**b**)

Figure 5. Reference and actual inductor currents when (**a**) 2ω suppression is not activated, (**b**) 2ω suppression is activated.

2.2.3. Gate Signal Generation

The presented block diagram in Figure 3c illustrates the gate signal generation scheme. To generate gate signals for switches of NPC-qZSI, the level shifted pulse width modulation approach is utilized.

The output of Lyapunov-function-based control block constitutes the source for the PWM signal generation process. The switching functions (modulation signals) should have 180° phase difference as seen in Figure 3c. To generate the PWM signals, the modulation signals should be compared with the level-shifted triangular signals. To do that, the carrier signals (Car1 and Car2), are generated which have the same phase shift, but are shifted vertically from each other.

Although the single-phase NPC-qZSI, which is illustrated in Figure 1, consists of eight switching devices, four switching signals are required to generate three different voltage levels. The generated switching signals ensure that the NPC-qZSI operates in buck mode. To allow the inverter to operate in boost mode, the shoot-through state should be considered in the gate signal generation scheme. It can be seen that the $\mathbf{d}_{ST}$ is obtained from dc-side control loop. To combine non-shoot through duty ratio and $\mathbf{d}_{ST}$, primitive logic gates are used. The switching devices on the first leg are turned-on when either Car1 is greater than $\mathbf{d}_{ST}$ or Car2 is greater than $\mathbf{d}_{ST} - 1$. The shoot-through state generation can be expressed as

$$If \begin{pmatrix} Car1 > \mathbf{d}_{ST} \\ OR \\ Car2 > \mathbf{d}_{ST} - 1 \end{pmatrix} then\ turn\ on\ S_{1a} - S_{4a}. \tag{40}$$

3. Results and Discussion

The proposed control idea and theoretical considerations are verified experimentally with a 2.5 kW grid-connected 3L-NPC-qZSI prototype. The system and control parameters are shown in Table 1.

Table 1. System and Control Parameters.

Parameter	Value
NPC-qZSI	
Input dc voltage (V_{in})	200 V
qZS network inductances ($L_1 - L_4$)	0.5 mH
qZS network capacitances ($C_1 - C_4$)	470 µF
Filter inductance (L_i, L_o)	1.5, 0.5 mH
Filter resistance (R_i, R_o)	0.1, 0.05 Ω
Filter capacitance (C_f)	22 µF
Grid voltage (v_g)	220 Vrms
AC-Side Controller	
Proportional gain (K_p)	5
Resonant gain (K_r)	1000
Control gains (K_c, K_v)	−0.0008, 0.875
DC-Side Controller	
Proportional gains (K_{P1}, K_{P2})	1.72, 1.2
Integrator gains (K_{I1}, K_{I2})	3.03, 2.1
Control gain (K_ω)	20

Figure 6 shows the steady-state experimental results of dc- and ac-side variables. The reference capacitor voltage (V^*_{C2} and V^*_{C3}) is 175 V and the reference grid current amplitude (i^*_2) is 10 A (max) during this test. It is obvious that the grid current (i_2) is in phase with the grid voltage (v_g). The measured THD of the grid current is 2.2% which is reasonably small and within the international standards for grid-connected inverters (see Figure 6b). It can be seen that the capacitor voltages are $V_{C2} = V_{C3} = 175$ V and $V_{C1} = V_{C4} = 75$ V. The dc-link voltage (V_{PN}), which is sum of the capacitor voltages, is 500 V. This result verifies that experimental results are are in good agreement with the theoretical analysis, which are presented in Section 2.1. Furthermore, the inductor current (I_{L1}) is continuous and 2ω ripple is eliminated by the proposed approach, which reduces the stress in the qZS network. It is important to note that 2ω ripple is eliminated only in the inductor currents not in the capacitors and dc-link voltages. However, the magnitude of these ripples are very small and depend on the qZS network design.

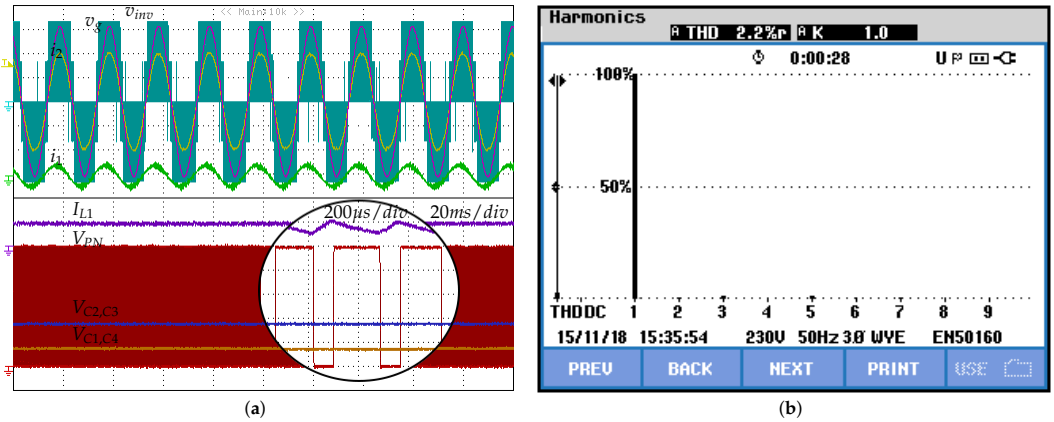

(**a**) (**b**)

Figure 6. Experimental results of the steady-state analysis. (**a**) ac and dc side variables; (**b**) Harmonic spectrum of grid current. ($i_1 = 20$ A/div, $i_2 = 5$ A/div, $v_g = 100$ V/div, $v_{inv} = 150$ V/div, $I_{L1} = 10$ A/div, $V_{C1-C4}, V_{PN} = 100$ V/div).

Figure 7 presents the steady-state results of without and with the 2ω ripple suppression technique. Please note that all system parameters are kept exactly the same for both tests. Figure 7a shows the experimental results when the dotted and highlighted part in

Figure 3b is disabled. It can be seen that the qZS inductor has around 4 A peak-to-peak 2ω ripple current. The relevant fast Fourier transform (FFT) analysis in Figure 7c shows that the inductor current contains the DC component as well as 100 Hz (2ω) ripple current component. On the other hand, Figure 7b shows the experimental results when the dotted and highlighted part in Figure 3b is enabled. Comparing Figure 7a with Figure 7b, one can see that the 2ω ripple on the inductor currents is eliminated by the proposed dc-side controller. In addition, the relevant FFT analysis in Figure 7d shows that the inductor current does not contain 100 Hz (2ω) ripple current component. Although there are high frequency components on the inductor current, their amplitudes are very low and can be neglected.

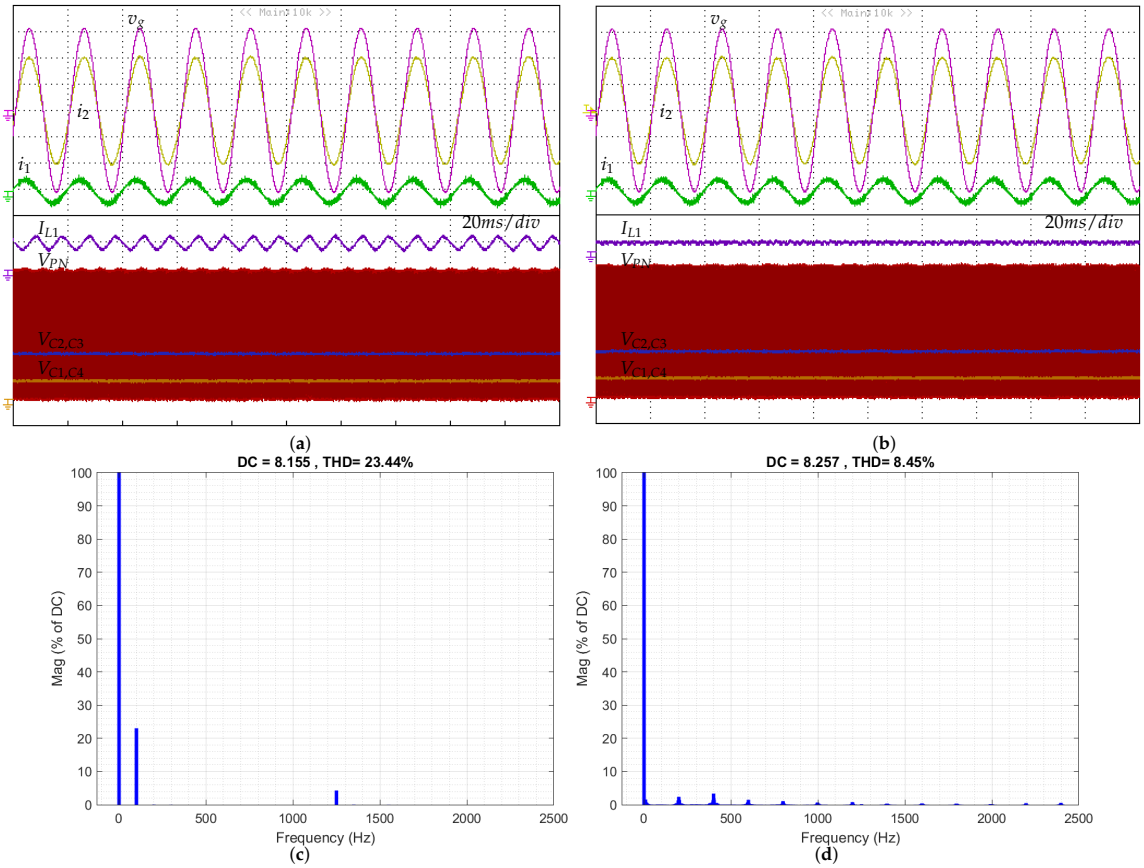

Figure 7. (**a**) Experimental steady-state results without double-line frequency reduction, (**b**) Experimental steady-state results with double-line frequency reduction, (**c**) Simulated spectrum of I_{L1} in part (**a**), and (**d**) Simulated spectrum of I_{L1} in part (**b**). ($i_1 = 20$ A/div, $i_2 = 5$ A/div, $v_g = 100$ V/div, $I_{L1} = 10$ A/div, $V_{C1-C4}, V_{PN} = 100$ V/div).

Figure 8a presents the transient responses of ac-side variables. Please note that during this test the V_{C2}^* and V_{C3}^* are constant and their values are 175 V. The initial grid current reference amplitude (i_2^*) is 5 A. Then, the i_2^* is stepped up from 5 to 10 A. It can be seen that the proposed control strategy shows a fast transient response to this abrupt reference variation without endangering the stability and damping. Although there are oscillations on the dc-side variables, they were damped in a short time (less than 60 ms) by the controller.

To test the transient performance of the dc-side controller, the capacitor voltage reference is stepped up from 150 to 175 V as shown in Figure 8b. It can be seen that initial capacitor voltages are $V_{C2} = V_{C3} = 150$ V and $V_{C1} = V_{C4} = 50$ V, which are consistent with the theoretical calculations. Results of this test show that the capacitor voltages follow their references accurately and reasonably small rising and settling times. Please note that the dynamic response on the dc-side does not affect the ac side operation.

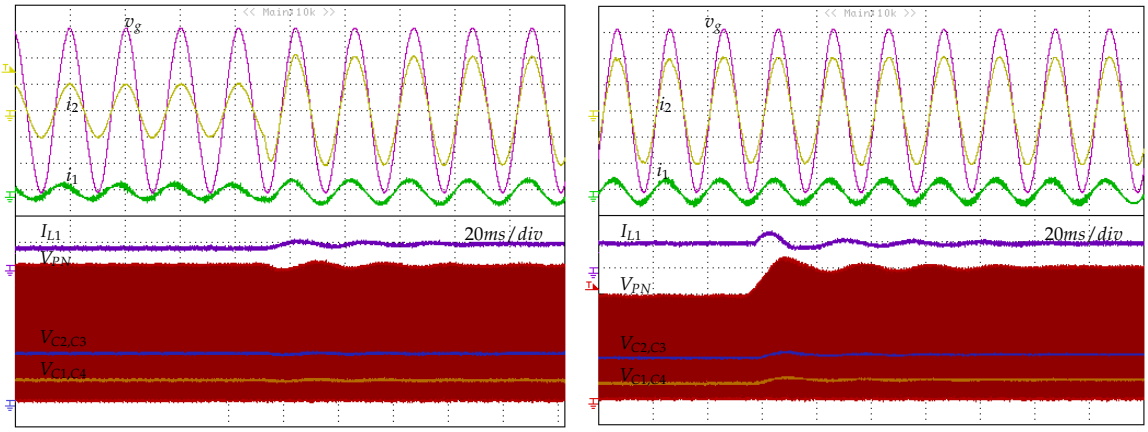

Figure 8. Experimental result of the dynamic response. (**a**) step on the grid current; (**b**) step on the capacitor voltage ($i_1 = 20$ A/div, $i_2 = 5$ A/div, $v_g = 100$ V/div, $I_{L1} = 10$ A/div, $V_{C1-C4}, V_{PN} = 100$ V/div).

Figure 9 shows the steady-state results obtained with $K_v = 0.15$. It should be noted that the other control parameters are exactly the same as in previous results. These results reveal that the performance of the closed-loop system in the ac-side is adversely affected when K_v is decreased. The main reason of this degradation comes from the fact that some poles are placed close to the imaginary axis.

To verify the proposed method under different power factor, the simulation studies were performed. The performance of the system under lagging, unity, and leading power factors with and without 2ω ripple reduction technique are shown in Figure 10a–c, respectively. In these results, while the active power is denoted by P_g, the reactive power is denoted by Q_g. Furthermore, the relevant FFT analysis of these operation modes are presented in Figure 11. The results show that the inductor current does not contain 100 Hz (2ω) ripple current component when the 2ω ripple reduction technique is enabled. Although there are high frequency components on the inductor current when the 2ω ripple reduction technique is disabled, their amplitudes are very low and can be neglected. To sum up, the results show that the performance of the 2ω ripple reduction technique is satisfactory for all operating conditions.

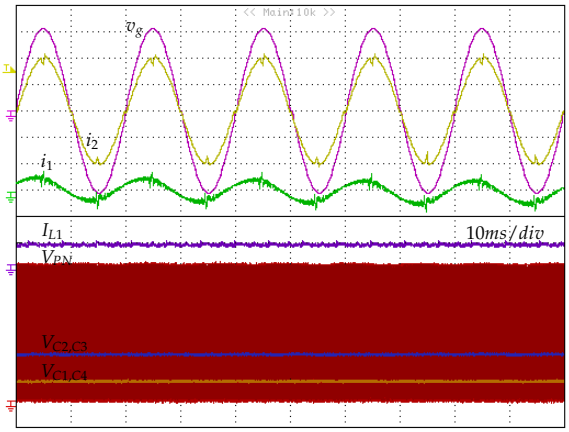

Figure 9. Experimental results when $K_v = 0.15$ ($i_1 = 20$ A/div, $i_2 = 5$ A/div, $v_g = 100$ V/div, $I_{L1} = 10$ A/div, $V_{C1-C4}, V_{PN} = 100$ V/div).

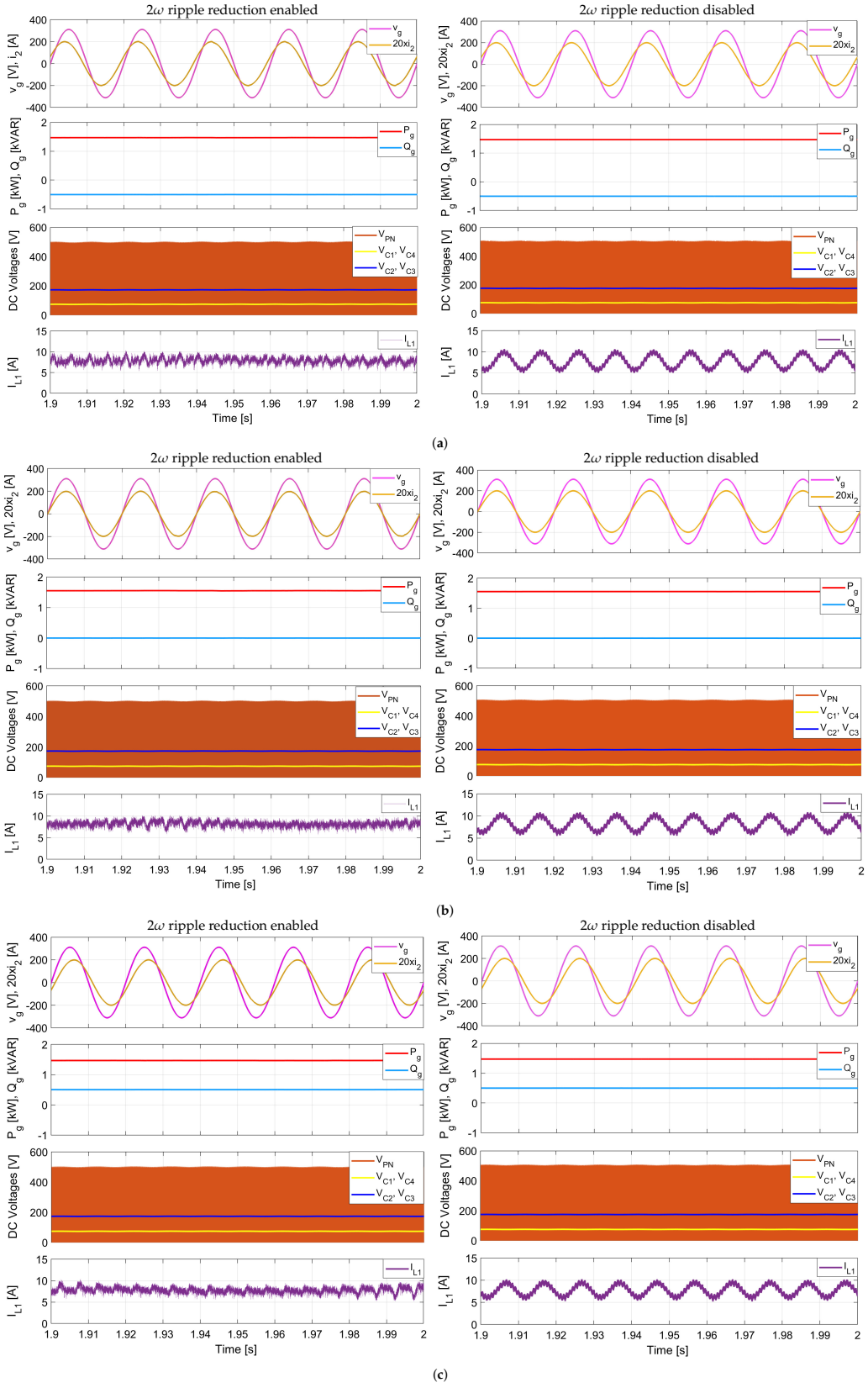

Figure 10. Simulation results of different power factors with and without the 2ω reduction technique; (**a**) P_g = 1.5 kW, Q_g = −0.5 kVAR; (**b**) P_g = 1.5 kW, Q_g = 0 kVAR; (**c**) P_g = 1.5 kW, Q_g = +0.5 kVAR.

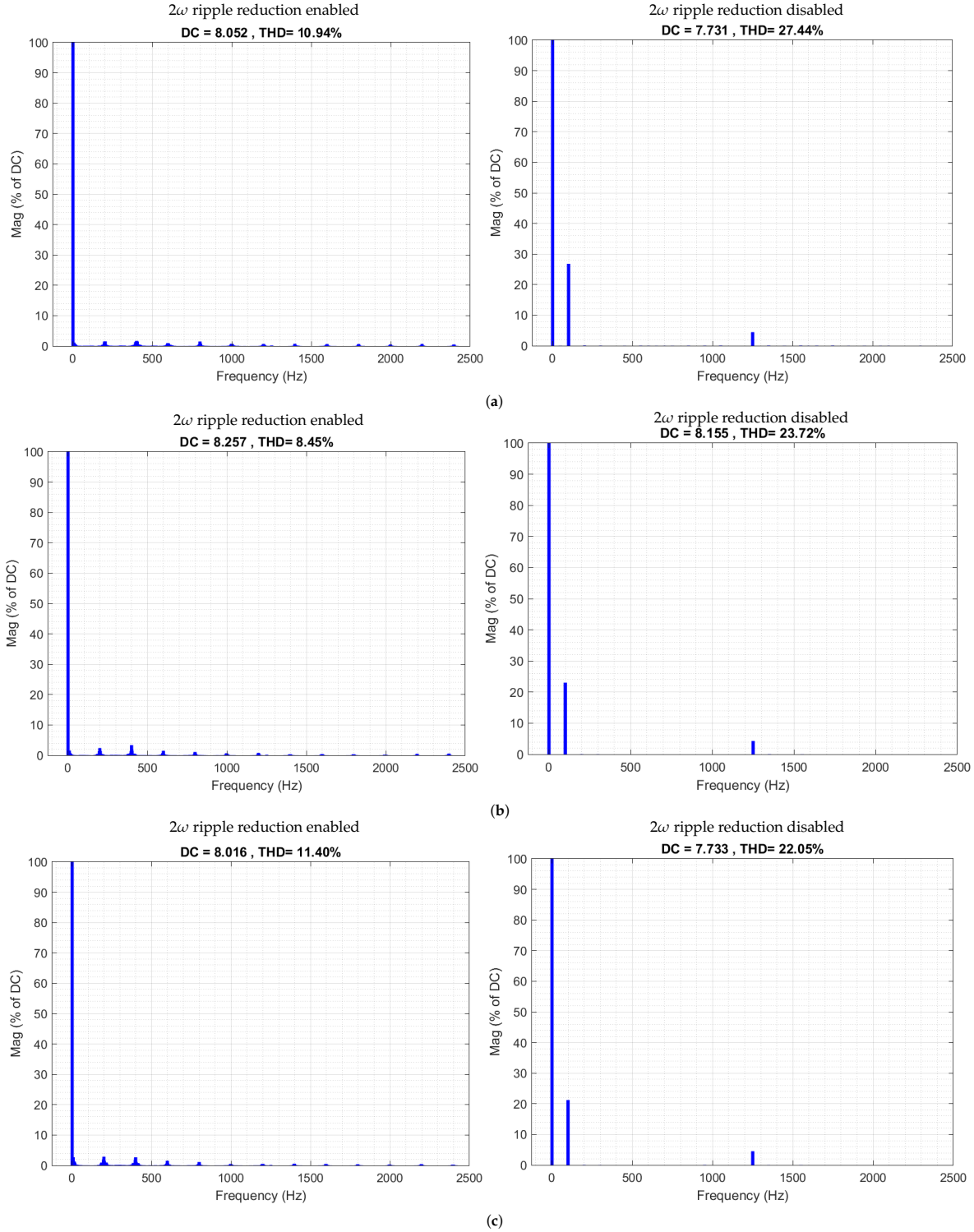

Figure 11. Simulated spectrum of I_{L1} with respect to Figure 10; (**a**) P_g=1.5 kW, Q_g = −0.5 kVAR; (**b**) P_g = 1.5 kW, Q_g = 0 kVAR; (**c**) P_g = 1.5 kW, Q_g = +0.5 kVAR.

The advantages and disadvantages of the existing ac-side control methods and the proposed control method are summarized in Table 2. According to the comparison in Table 2, the proposed control method offers advantages in terms of fast dynamic response, strengthened stability, reduced number sensors, excellent resonance damping, zero steady-state error and low THD in grid current.

Table 2. Existing AC-side control methods compared with the proposed control method.

Comparison Category	[14]	[11–13]	[15]	[16]	[18,19]	Proposed Control
Type of damping	Passive damping	VR-based active damping	VR-based active damping	VR-based active damping	Filter-based active damping	VR-based active damping
Advantages	[14]: Easy implementation [11–13]: Easy implementation, fast dynamic response, strong robustness and disturbance rejection [15]: Fast dynamic response, extensive stability analysis, requires two sensors [16]: Easy implementation, fast dynamic response, low THD in i_2 [18,19]: Requires one sensor **Proposed control:** Fast dynamic response, strengthened stability, requires two sensors, zero steady-state error and low THD in i_2, and very good damping feature					
Disadvantages	[14]: Additional power losses, reduced efficiency, and not reliable [11–13]: Chattering and variable-switching frequency, [13]: Requires three sensors [15]: Sensitive to parameter variations, complicated implementation, high THD and steady-state error in i_2 [16]: Fixed switching frequency with additional computation, no stability analysis, requires three sensors [18,19]: Sensitive to parameter variations and disturbances **Proposed control:** Increased computations					

4. Conclusions

In this study, a high-performance control technique based on Lyapunov's stability theory for a single-phase neutral-point-clamped quasi-impedance source inverter was proposed. The Lyapunov function based control is employed to regulate the inverter output current, whereas the proportional resonant controller is used to produce the reference of the inverter output current that is needed in the Lyapunov function based control. Use of proportional resonant controller ensures the zero steady-state error in the grid current.

It is shown that the modified simple boost control technique eliminates the double-line frequency ripple in the quasi-impedance source inductor currents and minimizes the double-line frequency ripples in the quasi-impedance source capacitor voltages. The proposed control technique considerably reduces the inverter size, weight, and cost as well as increases overall system efficiency since the required inductances and capacitances sizes are lower.

Experimental results obtained from a 2.5 kW neutral-point-clamped quasi-impedance source inverter prototype are presented to validate the performance of the controller under various operating conditions, including steady-state and transient responses. The results show that the proposed Lyapunov function based control has a fast response and nearly zero steady-state error. Furthermore, the proposed modified simple boost control technique eliminates the ripples on the inductances and minimizes the ripples on the capacitors.

Author Contributions: The research presented in this paper was a collaborative effort among both authors. S.B. and H.K. conceived, implemented, and got the results along with the paper write-up. S.B. and H.K. wrote the paper and discussed the results. All authors have read and agreed to the published version of the manuscript.

Funding: The publication of this article was funded by the Qatar National Library.

Acknowledgments: The publication of this article was funded by the Qatar National Library.

Conflicts of Interest: The authors declare no conflict of interest.

Nomenclature

The following abbreviations and nomenclature are used in this manuscript:

Abbreviations	
AC	Alternating current
DC	Direct current
MI	Multilevel inverters
NPC	Neutral point clamped
NPC-qZSI	Neutral point clamped quasi-impedance source inverter
PI	Proportional-integral
PID	Proportional-integral-derivative
PR	Proportional resonant
PV	Photovoltaic
qZSI	quasi-impedance source inverter
THD	Total harmonic distortion
VR	Virtual resistor
Nomenclature	
B	Boost factor
C_f	The filter capacitance (μF)
$C_1 - C_4$	qZS network capacitances (μF)
$\mathbf{d_{ST}}$	Shoot-through duty-cycle (%)
$\mathbf{d}$	The switching function
d_{ss}	The steady state term of the switching function
d_p	The perturbed term of the switching function
G_{PR}	The transfer function of proportional resonant controller
i_{L1}	Inductor current (A)
I_1	The output current(A)
K_p	AC-side proportional gain
K_r	AC-side resonant gain
K_c, K_v	AC-side control gains
K_{p1}, K_{p2}	DC-side proportional gains
K_{I1}, K_{I2}	DC-side integral gains
K_ω	DC-side control gain
$L_1 - L_4$	qZS network inductances (mH)
L_i, L_o	The filter inductances (mH)
P_o	The inverter output power (W)
R_i, R_o	The resistances of filter inductances (ohm)
T_0	Shoot-through period (sec)
T_1	Non-shoot-through period (sec)
V_{PN}	DC-link voltage (V)
v_{inv}	The output voltage (V)
V_{in}	Input dc voltage (V)
V_{L1-L4}	The voltage across the inductors (V)
V_{C1-C4}	The voltage across the capacitors (V)
v_C	The filter capacitor voltage (V)
ω	Fundamental angular frequency (rad/s)
θ	Phase angle (rad)
2ω	Double-line frequency (rad/s)

References

1. Abu-Rub, H.; Malinowski, M.; Al-Haddad, K. *Power Electronics for Renewable Energy Systems, Transportation and Industrial Applications*; A John Wiley & Sons Ltd.: Hoboken, NJ, USA, 2014.
2. Rodriguez, J.; Lai, J.S.; Peng, F.Z. Multilevel inverters: A survey of topologies, controls, and applications. *IEEE Trans. Ind. Electron.* **2002**, *49*, 724–738. [CrossRef]

3. Husev, O.; Roncero-Clemente, C.; Romero-Cadaval, E.; Vinnikov, D.; Stepenko, S. Single phase three-level neutral-point-clamped quasi-Z-source inverter. *IET Power Electron.* **2015**, *8*, 1–10. [CrossRef]
4. Bayhan, S.; Abu-Rub, H.; Balog, R.S. Model Predictive Control of Quasi-Z-Source Four-Leg Inverter. *IEEE Trans. Ind. Electron.* **2016**, *63*, 4506–4516. [CrossRef]
5. Makovenko, E.; Husev, O.; Roncero-Clemente, C.; Romero-Cadaval, E.; Blaabjerg, F. Single-phase 3L PR controlled qZS inverter connected to the distorted grid. In Proceedings of the 2016 10th International Conference on Compatibility, Power Electronics and Power Engineering (CPE-POWERENG), Bydgoszcz, Poland, 29 June–1 July 2016; pp. 234–239.
6. Husev, O.; Roncero-Clemente, C.; Romero-Cadaval, E.; Vinnikov, D.; Jalakas, T. Three-level three-phase quasi-Z-source neutral-point-clamped inverter with novel modulation technique for photovoltaic application. *Electr. Power Syst. Res.* **2016**, *130*, 10–21. [CrossRef]
7. Husev, O.; Stepenko, S.; Roncero-Clemente, C.; Romero-Cadaval, E.; Strzelecki, R. Experimental Investigation of high frequency 3L-NPC qZS inverter for photovoltaic application. In Proceedings of the IECON 2013—39th Annual Conference of the IEEE Industrial Electronics Society, Vienna, Austria, 10–13 November 2013; pp. 5969–5974.
8. Song, W.; Ma, J.; Zhou, L.; Feng, X. Deadbeat Predictive Power Control of Single-Phase Three-Level Neutral-Point-Clamped Converters Using Space-Vector Modulation for Electric Railway Traction. *IEEE Trans. Power Electron.* **2016**, *31*, 721–732. [CrossRef]
9. Vazquez, S.; Rodriguez, J.; Rivera, M.; Franquelo, L.G.; Norambuena, M. Model Predictive Control for Power Converters and Drives: Advances and Trends. *IEEE Trans. Ind. Electron.* **2017**, *64*, 935–947. [CrossRef]
10. Evran, F. Plug-in repetitive control of single-phase grid-connected inverter for AC module applications. *IET Power Electron.* **2017**, *10*, 47–58. [CrossRef]
11. Komurcugil, H.; Ozdemir, S.; Sefa, I.; Altin, N.; Kukrer, O. Sliding-Mode Control for Single-Phase Grid-Connected LCL-Filtered VSI With Double-Band Hysteresis Scheme. *IEEE Trans. Ind. Electron.* **2016**, *63*, 864–873. [CrossRef]
12. Altin, N.; Ozdemir, S.; Komurcugil, H.; Sefa, I. Sliding-Mode Control in Natural Frame with Reduced Number of Sensors for Three-Phase Grid-Tied LCL-Interfaced Inverters. *IEEE Trans. Ind. Electron.* **2018**, *66*, 2903–2913. [CrossRef]
13. Hao, X.; Yang, X.; Liu, T.; Huang, L.; Chen, W. A Sliding-Mode Controller With Multiresonant Sliding Surface for Single-Phase Grid-Connected VSI With an LCL Filter. *IEEE Trans. Power Electron.* **2013**, *28*, 2259–2268. [CrossRef]
14. Pena-Alzola, R.; Liserre, M.; Blaabjerg, F.; Sebastian, R.; Dannehl, J.; Fuchs, F.W. Analysis of the Passive Damping Losses in LCL-Filter-Based Grid Converters. *IEEE Trans. Power Electron.* **2013**, *28*, 2642–2646. [CrossRef]
15. Eren, S.; Pahlevaninezhad, M.; Bakhshai, A.; Jain, P.K. Composite Nonlinear Feedback Control and Stability Analysis of a Grid-Connected Voltage Source Inverter With LCL Filter. *IEEE Trans. Ind. Electron.* **2013**, *60*, 5059–5074. [CrossRef]
16. Komurcugil, H.; Bayhan, S.; Abu-Rub, H. Variable- and Fixed-Switching-Frequency-Based HCC Methods for Grid-Connected VSI With Active Damping and Zero Steady-State Error. *IEEE Trans. Ind. Electron.* **2017**, *64*, 7009–7018. [CrossRef]
17. Loh, P.; Holmes, D.G. Analysis of multiloop control strategies for LC/CL/LCL-filtered voltage-source and current-source inverters. *IEEE Trans. Ind. Appl.* **2005**, *41*, 644–654. [CrossRef]
18. Dannehl, J.; Liserre, M.; Fuchs, F.W. Filter-Based Active Damping of Voltage Source Converters With LCL Filter. *IEEE Trans. Ind. Electron.* **2011**, *58*, 3623–3633. [CrossRef]
19. Yao, W.; Yang, Y.; Zhang, X.; Blaabjerg, F.; Loh, P.C. Design and Analysis of Robust Active Damping for LCL Filters Using Digital Notch Filters. *IEEE Trans. Power Electron.* **2017**, *32*, 2360–2375. [CrossRef]
20. Liu, F.; Zhou, Y.; Duan, S.; Yin, J.; Liu, B.; Liu, F. Parameter Design of a Two-Current-Loop Controller Used in a Grid-Connected Inverter System With LCL Filter. *IEEE Trans. Ind. Electron.* **2009**, *56*, 4483–4491.
21. Zhang, B.; Li, Y.; Yang, X.; Liu, Y.; Guo, X.; Chen, J. Lyapunov Function Based Control Strategy for Hybrid Active Power Filter. In Proceedings of the 2017 2nd International Conference on Cybernetics, Robotics and Control (CRC), Chengdu, China, 21–23 July 2017; pp. 94–100.
22. Rezkallah, M.; Sharma, S.K.; Chandra, A.; Singh, B.; Rousse, D.R. Lyapunov Function and Sliding Mode Control Approach for the Solar-PV Grid Interface System. *IEEE Trans. Ind. Electron.* **2017**, *64*, 785–795. [CrossRef]
23. Sefa, I.; Ozdemir, S.; Komurcugil, H.; Altin, N. Comparative study on Lyapunov-function-based control schemes for single-phase grid-connected voltage-source inverter with LCL filter. *IET Renew. Power Gener.* **2017**, *11*, 1473–1482. [CrossRef]
24. Komurcugil, H.; Bayhan, S.; Abu-Rub, H. Lyapunov-function based control approach with cascaded PR controllers for single-phase grid-tied LCL-filtered quasi-Z-source inverters. In Proceedings of the 2017 11th IEEE International Conference on Compatibility, Power Electronics and Power Engineering (CPE-POWERENG), Cadiz, Spain, 4–6 April 2017; pp. 510–515.
25. Komurcugil, H.; Altin, N.; Ozdemir, S.; Sefa, I. Lyapunov-Function and Proportional-Resonant-Based Control Strategy for Single-Phase Grid-Connected VSI With LCL Filter. *IEEE Trans. Ind. Electron.* **2016**, *63*, 2838–2849. [CrossRef]
26. Liu, Y.; Abu-Rub, H.; Ge, B. Z-Source Quasi-Z-Source Inverters: Derived Networks, Modulations, Controls, and Emerging Applications to Photovoltaic Conversion. *IEEE Indus. Electron. Mag.* **2014**, *8*, 32–44. [CrossRef]
27. Liu, Y.; Abu-Rub, H.; Ge, B.; Blaabjerg, F.; Ellabban, O.; Poh, C.L. *Impedance Source Power Electronic Converters*; IEEE Press: New York, NY, USA; A John Wiley & Sons Ltd.: Hoboken, NJ, USA, 2016.
28. Bayhan, S.; Trabelsi, M.; Abu-Rub, H. Model predictive control based current ripple damping in single-phase quasi-impedance-source inverter. In Proceedings of the 2017 19th European Conference on Power Electronics and Applications (EPE'17 ECCE Europe), Warsaw, Poland, 11–15 September 2017.

29. Ge, B.; Liu, Y.; Abu-Rub, H.; Balog, R.S.; Peng, F.Z.; Sun, H.; Li, X. An Active Filter Method to Eliminate DC-Side Low-Frequency Power for a Single-Phase Quasi-Z-Source Inverter. *IEEE Trans. Ind. Electron.* **2016**, *63*, 4838–4848. [CrossRef]
30. Ge, B.; Liu, Y.; Abu-Rub, H.; Balog, R.S.; Peng, F.Z.; McConnell, S.; Li, X. Current Ripple Damping Control to Minimize Impedance Network for Single-Phase Quasi-Z Source Inverter System. *IEEE Trans. Ind. Inf.* **2016**, *12*, 1043–1054. [CrossRef]
31. Liang, W.; Liu, Y.; Ge, B.; Abu-Rub, H.; Balog, R.S.; Xue, Y. Double-Line-Frequency Ripple Model, Analysis, and Impedance Design for Energy-Stored Single-Phase Quasi-Z-Source Photovoltaic System. *IEEE Trans. Ind. Electron.* **2018**, *65*, 3198–3209. [CrossRef]
32. Bayhan, S.; Kakosimos, P.; Abu-Rub, H.; Rodriguez, J. Model predictive control of five-level H-bridge neutral-point-clamped qZS inverter. In Proceedings of the IECON 2016—42nd Annual Conference of the IEEE Industrial Electronics Society, Florence, Italy, 23–26 October 2016; pp. 5971–5976.
33. Bayhan, S.; Komurcugil, H.; Abu-Rub, H.; Liu, Y. A Lyapunov-function based control strategy for for single-phase neutral-point-clamped quasi-impedance source inverter with *LCL* filter. In Proceedings of the IECON 2018—44th Annual Conference of the IEEE Industrial Electronics Society, Washington, DC, USA, 21–23 October 2018; pp. 3695–3699.